High-Resolution Scanning Tunneling Microscopy of Fully Hydrated Ripple-Phase Bilayers

J. T. Woodward IV* and J. A. Zasadzinski#
*Department of Physics and #Department of Chemical Engineering, University of California, Santa Barbara, California 93106-5080 USA

ABSTRACT A modified freeze-fracture replication technique for use with the scanning tunneling microscope (STM) has provided a quantitative, high-resolution description of the waveform and amplitude of rippled bilayers in the $P_{\beta'}$ phase of dimyristoylphosphatidylcholine (DMPC) in excess water. The ripples are uniaxial and asymmetrical, with a temperature-dependent amplitude of 2.4 nm near the chain melting temperature that decreases to zero at the chain crystallization temperature. The wavelength of 11 nm does not change with temperature. The observed ripple shape and the temperature-induced structural changes are not predicted by any current theory. Calibration and reproducibility of the STM/replica technique were tested with replicas of well-characterized bilayers of cadmium arachidate on mica that provide regular 5.5-nm steps. STM images were analyzed using a cross-correlation averaging program to eliminate the effects of noise and the finite size and shapes of the metal grains that make up the replica. The correlation averaging allowed us to develop a composite ripple profile averaged over hundreds of individual ripples measured on different samples with different STM tips. The STM/replica technique avoids many of the previous artifacts of biological STM imaging and can be used to examine a variety of periodic hydrated lipid and protein samples at a lateral resolution of about 1 nm and a vertical resolution of about 0.3 nm. This resolution is superior to conventional and tapping mode AFM of soft biological materials; the technique is substrate-free, and the conductive and chemically uniform replicas make image interpretation simple and direct.

INTRODUCTION

The self-assembly of phospholipid bilayers has been studied extensively as a simple biophysical model of the cell membrane (Singer and Nicolson, 1972; Jacobson et al., 1995). The packing of the bilayers, in turn, forms a rich variety of liquid crystalline phases (Tardieu et al., 1972; Janiak et al., 1979; Wack and Webb, 1989). Lipid bilayer morphologies have taken on an additional significance in the light of recent experiments that show that the lipid membrane is more than a passive matrix for biologically active proteins (Singer and Nicolson, 1972; Jacobson et al., 1995); protein function can be modified by the composition, phase, and local structure of the lipids (Keller et al., 1993).

However, the structure of a lyotropic liquid crystalline material is extremely difficult to characterize by typical structural probes. X-ray or neutron scattering methods usually cannot provide unambiguous assignments as these materials are difficult to align, domain sizes and correlation lengths are small, and thermal fluctuations tend to eliminate higher order reflections, especially in excess water (Sirota et al., 1988; Mortensen et al., 1988; Hentschel and Rustichelli, 1991; Matuoka et al., 1994; Katsaras and Raghunathan, 1995). Better results are obtained by using high-intensity synchrotron sources (Wack and Webb, 1989; Sirota et al., 1988) along with computer-intensive fitting procedures to back out structural profiles (Sun et al., 1996; Nagle et al., 1996). As an alternative and more visual approach, freeze-fracture electron microscopy has been used to investigate membrane structure and has led to a general acceptance of the fluid mosaic model of cell membranes (Branton, 1966; Singer and Nicolson, 1972). Freeze-fracture electron microscopy has since proved to be equally valuable in determining morphological changes that accompany phase transitions in lyotropic (Kleman et al., 1977; Luna and McConnell, 1977; Gulik-Krzywicki and Costello, 1978; Ruppel and Sackman, 1983; Zasadzinski and Meyer, 1986; Zasadzinski et al., 1986; Zasadzinski and Bailey, 1989) and thermotropic liquid crystals (Costello et al., 1984; Zasadzinski et al., 1986; Ihn et al., 1992) and other complex fluids such as microemulsions (Jahn and Strey, 1988). However, quantitative analysis of freeze-fracture images to determine structural parameters has been limited because of inherent difficulties in extracting three-dimensional structural information from micrographs (Krbecek et al., 1979; Zasadzinski and Bailey, 1989).

The scanning tunneling microscope (STM) (Binnig et al., 1982; Quate, 1986; Hansma and Tersoff, 1987) offers new ways of imaging surfaces in three dimensions; however, easily understood and reproducible STM images of biological materials are quite difficult to obtain, as such materials are nonconductive and soft (Amrein et al., 1988, 1989; Foster et al., 1988; Foster and Frommer, 1988; Hansma et al., 1988; Hörber et al., 1988; Lang et al., 1988; Travaglini et al., 1987). Imaging with any probe microscope invariably involves mounting the sample on a substrate, which is often accompanied by its own set of artifacts (Hörber et al., 1988; Lang et al., 1988; Clemmer and Beebe, 1991; Clemmer et

Received for publication 30 August 1996 and in final form 1 November 1996.

Address reprint requests to Dr. Joseph A. Zasadzinski, Department of Chemical Engineering, University of California, Santa Barbara, CA 93106. Tel.: 805-893-4769; Fax: 805-893-4731; gorilla@squid.ucsb.edu.

Dr. Woodward's present address is Department of Chemistry, Tulane University, New Orleans, LA 70118.

0006-3495/97/02/964/13 $2.00

al., 1992; Patrick and Beebe, 1993). Much of the initial promise of biological STM has proved false; artifacts abound in the literature because direct STM images of insulating materials are difficult to understand, based on any reasonable model of electron tunneling (Lang et al., 1988; Lindsay and Barris, 1988; Spong et al., 1989; Clemmer and Beebe, 1991). However, recent work suggests that many images of biomaterials are actually maps of thin layers of loosely bound water with sufficient conductivity to provide a current for imaging (Sonnenfeld and Hansma, 1987; Yuan et al., 1991; Guckenberger et al., 1994). A better explanation might be that images of biological materials are primarily due to electrochemical reactions at the STM tip, as in the scanning electrochemical microscope (Arca et al., 1994). However, such explanations are qualitative, resolution is poor, and it is difficult to directly relate image contrast to features in the image.

At present, most biological surfaces are imaged via atomic force microscopy (Binnig et al., 1986; Gould et al., 1988; Hansma et al., 1988; Zasadzinski et al., 1994a,b; Mou et al., 1994; Hui et al., 1995; Shao and Yang, 1995) or one of its recent variants, including noncontact or tapping AFM (Manne et al., 1994; Hansma et al., 1994; Radmacher et al., 1994), lateral or friction force microscopy (Meyer et al., 1992; Overney et al., 1992), or specific chemical or biochemical microscopy (Florin et al., 1994; Frisbie et al., 1994). There are many benefits of these techniques, the most important being 1) nonconductors are readily imaged; 2) imaging can be done under solvents or in near in vivo conditions; and 3) specific chemical information can be obtained via tip-sample interactions. However, there are several drawbacks to each of these techniques, the most important being difficulty in relating specific forces to structural features. Moreover, all of these force microscopy techniques are still limited to imaging materials bound to a substrate. In practice, AFM resolution appears to be inferior to the STM, especially on rough surfaces, most likely because of the quite different nature of the tip-sample interactions. The STM tip is inherently of higher resolution because of the exponential dependence of tunneling current on separation as opposed to the generally quite complicated fall off of force with separation in the AFM.

An alternative to the various AFM techniques that avoids direct STM imaging of biomaterials is coating nonconductive surfaces with metal layers to make them conductive, then imaging with the STM (Travaglini et al., 1987; Amrein et al., 1988; Zasadzinski et al., 1988; Obcemea and Vidic, 1992; Hatta et al., 1993; Woodward and Zasadzinski, 1994, 1996a; Muller-Reichert et al., 1996). Conventional freeze-fracture techniques, which are extremely useful for imaging biological membranes, suspensions, etc. in excess water with TEM, can be modified for the STM. Imaging metal replicas with the STM removes many of the common problems associated with biological STM and/or AFM—the replica is conductive and chemically homogeneous and the sample is prepared while fully hydrated and in bulk solution.

Freeze-fracture replication is a four-step thermal fixation technique originally developed by Steere (1957) to image thermally fixed cells and suspensions. A thin layer of sample is trapped between two thin copper plates, quickly frozen, and then fractured under vacuum (Zasadzinski and Bailey, 1989). The fracture surface is replicated by evaporating a thin metal layer at an angle with respect to the fracture surface; the metal film is followed by a thicker carbon layer for strength. Any remaining portions of the original sample are cleaned off, and the replica is then examined in the TEM. In any individual replica of a nonrepetitive surface examined in the TEM, the lateral resolution is limited by the size of the metal film grains to about 2 nm (Woodward and Zasadzinski, 1996b). Image analysis techniques can remove some of the influence of the granularity of the replica, especially for periodic surfaces (Woodward et al., 1995). Vertical steps in the fracture surface as small as 0.5 nm can be detected because of the shadowing effects of the oblique metal deposition.

In principle, a platinum/carbon replica of a fracture surface is an ideal sample for STM imaging—it is highly conductive, chemically homogeneous, inert, and easily manipulated. However, imaging with the STM is fundamentally different from imaging with the TEM and requires some basic modifications of the freeze-fracture technique. The freeze-fracture STM techniques detailed in this paper are an alternative to conventional AFM imaging of soft or insulating surfaces, and can be used to prepare substrate-free samples for high-resolution imaging. In fact, this technique is the only scanning probe method amenable to suspensions or dispersions in solution. As we show here for the regular and repeating ripples of the $P_{\beta'}$ phase of DMPC in excess water, the combination of freeze-fracture replication, careful STM imaging in controlled environments, and correlation averaging image analysis can achieve a 1-nm lateral and 0.3-nm vertical resolution on substrate-free samples of biomembranes.

Saturated phosphatidylcholines (PCs) are present in many cell membranes and are the major component of human lung surfactant (Longo et al., 1993). Saturated PCs undergo three distinct structural transitions when dispersed in water: a subtransition, pretransition, and main transition separating the phases L_c, $L_{\beta'}$, $P_{\beta'}$, and L_α, respectively (Tardieu et al., 1972; Janiak et al., 1979; Wack and Webb, 1989). In the high-temperature L_α phase, the order within each bilayer is short range and the *trans-gauche* intramolecular order is low. The main transition is associated with lipid chain melting (Tardieu et al., 1972; Janiak et al., 1979). The bilayers are smooth and the molecules, on average, are normal to the bilayer—the symmetry is similar to the thermotropic smectic A phase. The $L_{\beta'}$ phase is characterized by flat bilayers with the lipid chains fully extended (all-*trans* configuration) and tilted with respect to the bilayer normal. The positional order appears to be short range and the orientational order longer range (Sirota et al., 1988). The low-temperature $L_{\beta'} \rightarrow L_c$ transition involves a modification of the chain packing and dehydration of the headgroups (Janiak et al., 1979).

However, a satisfactory explanation of the $P_{\beta'}$ phase remains a challenge. In the $P_{\beta'}$ phase, the lipid chains retain much of their all-*trans* configuration, and the molecules are packed into a two-dimensional hexagonal lattice with long-range orientational correlations (Janiak et al., 1979; Ruppel and Sackman, 1983; Zasadzinski and Schneider, 1987). The bilayers are characterized by regular three-dimensional corrugations, hence the common name of ripple phase. The temperature range over which the ripple phase occurs decreases with increasing hydrocarbon chain length, and the absolute temperature increases. For DMPC (14-carbon chains) the $P_{\beta'}$ phase exists from 14 to 24°C, and for dipalmitoylphosphatidylcholine (16-carbon chains), the $P_{\beta'}$ phase exists from 35 to 41.5°C; the $P_{\beta'}$ phase disappears for PCs longer than 20 carbons (Wack and Webb, 1989). X-ray diffraction and freeze-fracture electron microscopy find the ripple wavelength of DMPC in excess water to be about 11–12 nm (Tardieu et al., 1972; Luna and McConnell, 1977; Janiak et al., 1979; Ruppel and Sackman, 1983; Zasadzinski and Schneider, 1987; Zasadzinski et al., 1988; Wack and Webb, 1989). The wavelength of the ripple increases with increasing lipid chain length and decreases with increasing water content up to full hydration (Wack and Webb, 1989). Most studies have shown that the ripple wavelength is roughly constant at a given water fraction over the entire temperature range of the $P_{\beta'}$ phase (Mortensen et al., 1988; Matuoka et al., 1994). Whereas the wavelength of the ripples has been well established experimentally, estimates of the ripple amplitude range from about 0.5 to 5 nm (Janiak et al., 1979; Zasadzinski et al., 1988; Woodward and Zasadzinski, 1996a; Sun et al., 1996), and the shape of the ripples is unknown.

Models of the $P_{\beta'}$ phase fall into two broad classes: phenomenological models based on modulations of membrane thickness (Goldstein and Leibler, 1988; Cevc, 1991) or curvature (Doniach, 1979; Lubensky and MacKintosh, 1993) and molecular models based on packing frustration between the lipid headgroup and chains (Carlson and Sethna, 1987; McCullough and Scott, 1990; Scott and McCullough, 1991; Schwartz et al., 1994). The structural details of the corrugations are undetermined; some models assume a sinusoidal modulation (Doniach, 1979; Lubensky and MacKintosh, 1993), whereas others predict a more sawtooth modulation (Tardieu et al., 1972; Ruppel and Sackmann, 1983; Scott and McCullough, 1991; Hatta et al., 1993). To distinguish between these theories requires that the amplitude, waveform, and wavelength of the ripples be measured with sufficiently high resolution to determine the details of the modulation. The STM-freeze-fracture replication technique is the only way to image the ripple phase in excess water with sufficient resolution to determine these details.

MATERIALS AND METHODS

Platinum/carbon replicas of DMPC bilayers in excess water, equilibrated at 16, 18, 20, and 23°C, were prepared for both TEM and STM examination to determine the temperature dependence of the ripple amplitude, waveform, and wavelength (the $P_{\beta'}$ phase of DMPC exists from 14 to 24°C). For each sample, 200 mg of DMPC (Avanti Polar Lipids, Atlanta, GA) was added to 0.2 ml Milli-Q water (Millipore, Bedford, MA); the resulting 50% DMPC/50% water mixture ensured that the bilayers were fully hydrated and that any small water losses during sample preparation would not modify the ripple morphology (Wack and Webb, 1989). The samples were alternately centrifuged at low speed, vortexed, then heated at >30°C for at least 24 h to allow complete mixing. Films (10–50 μm thick) of the DMPC-water mixture were sandwiched between copper freeze-fracture planchettes (Baltech BUO-12-056T; Hudson, NH), then equilibrated at 100% relative humidity in a controlled environment chamber (Bailey et al., 1991; Bellare et al., 1988) at 23, 20, 18, or 16°C before rapid quenching in liquid propane cooled by liquid nitrogen. Sample cooling rates were estimated to be in excess of 10^4 C/s (Bailey and Zasadzinski, 1991).

Freeze-fracture replication was done in a Balzers 400K freeze-etch machine. After the samples were loaded into the freeze-etch machine, the samples were fractured at −170°C and 10^{-7} torr pressure. The TEM samples were immediately shadowed with 1.5 nm of Pt/C at a 45° angle relative to the surface, and the STM samples were coated normal to the surface while the sample table was rotated to ensure a continuous coating. A 15-nm-thick film of carbon was added to both Pt/C films to stabilize the shadowing film. Replicas for STM had an additional 0.5-μm-thick layer of silver deposited by sputtering to increase film rigidity. For proper interpretation of the replica, the sample material must be completely removed from the replica before viewing. In our laboratory, the cleaning method of Fetter and Costello (1985) has always given the best results. The cleaned replicas are collected on formvar-coated copper TEM grids for the TEM samples, or on fine mesh silver wire filter membranes (SPI Supplies, West Chester, PA) with a nominal 0.2-μm pore size for the STM samples. Replicas of each sample were examined first with TEM (JEM 100CXII) to determine replica quality and identify the ripple phase. STM (Digital Instruments, Santa Barbara, CA) imaging was done with a 12-μm scanning head in the constant current mode under a dry nitrogen atmosphere to eliminate capillary condensation from laboratory air. Typical imaging conditions were 100 mV bias voltage, 1.0 nA tunneling current, and a scan rate of 5.8 Hz. Each sample was examined with several different cut Pt/Ir tips to eliminate any systematic errors.

The vertical piezo of the STM was calibrated by measuring Pt/C replicas of bilayer steps of Langmuir-Blodgett films of cadmium arachidate. The calibration specimen surface consisted of bilayer islands of cadmium arachidate of 1–2 μm in extent that vary in height by a bilayer from adjacent areas (Schwartz et al., 1992a,b). The thickness of the bilayer is known from x-ray diffraction (Tippmann-Krayer et al., 1992) and AFM images to be 5.5 nm (Schwartz et al., 1992a,b). Replicas of these surfaces were made as described above. Step heights were measured by taking bearing plots of roughly equal areas on both sides of a step and taking the difference between the peak values to be the step height. In a dry nitrogen atmosphere, the images were stable for more than 1 h, and lateral and vertical feature dimensions were reproducible for hundreds of scans. Ten images taken with three different tips gave 28 bilayer height measurements. The measured mean height was used to calibrate the vertical piezo. Seventy percent of the measurements fell within 8% of the mean (Woodward and Zasadzinski, 1994). The variance was similar than that achieved when the bilayer steps were measured directly with the AFM (Garnaes et al., 1993). There was no significant difference in heights measured with different tips.

Modifications to freeze-fracture replication for STM imaging

There is a fundamental difference in the sample requirements for STM imaging as opposed to TEM imaging that required modifications to the traditional thin replicas used in freeze-fracture TEM. In our initial studies of freeze-fracture replicas with the STM, we found that the height information could be very erratic. Images of similar objects on the same replica could differ by more than a factor of 10 in apparent height (Woodward et al., 1991). Other times, the height of an object would grow or shrink with

continued scanning (Hansma et al., 1988; Woodward and Zasadzinski, 1994). The literature also includes a number of accounts of unusual height measurements on a variety of samples (Hallmark et al., 1987; Hansma and Tersoff, 1987). A number of theoretical models have proposed that specific quantum- and atomic-scale interactions can lead to amplifications in specific tip-sample systems (Tersoff and Lang, 1990; Ciraci et al., 1990; Yuan and Shao, 1990; Chen, 1992). Other theories propose that bulk compression by the scanning tip at regions of low conductivity or solid surface contamination could lead to amplifications of surface features (Soler et al., 1986; Mamin et al., 1986).

In most descriptions of scanning tunneling microscopy, there is no discussion of the physical coupling between the STM tip and sample, even though there are at least three significant interactions to consider when imaging is done in air: 1) electrostatic interaction due to the potential difference between the tip and sample, 2) van der Waals attraction, and 3) capillary attraction due to the Laplace pressure generated by the formation of a highly curved fluid meniscus connecting the tip and sample (Woodward et al., 1991; Woodward and Zasadzinski, 1994). These forces can cause the STM tip, while traversing a surface feature with an actual height, Z, to distort the surface being measured, resulting in an amplified height, Z^*. The role of capillary forces in scanning probe microscopy has been recognized in the AFM literature (Erlandsson et al., 1988; Weisenhorn et al., 1992; Blackman et al., 1990), but an appreciation of their importance during STM imaging has lagged (Yuan et al., 1991; Anselmetti et al., 1993; Guckenberger et al., 1994).

The forces that couple the STM tip to the sample can be modeled as a spring of spring constant k_1. A second spring of spring constant k_2 connects the sample to the STM base. Regardless of the functional form of k_1 and k_2, this combination of springs will amplify a surface feature of actual height Z by

$$Z^* = Z(k_1 + k_2)/k_2, \tag{1}$$

where Z^* is the height measured by the STM. In most applications in which the sample is a uniformly rigid solid firmly mounted to the base, k_2 is very large compared to k_1 and no amplification is expected (k_2 would be related to the bulk compressibility or elastic modulus of the sample being imaged; Mamin et al., 1986). However, if the sample is soft, nonuniform, or weakly connected to the base, as is often the case for organic or biological films, replicas, or even layered solids like highly oriented pyrolitic graphite (a common STM substrate), k_2 can be much less locally than k_1, leading to large amplifications (Patrick and Beebe, 1993).

Of the three interactions between tip and sample listed above, capillary condensation is by far the dominant interaction (Woodward and Zasadzinski, 1994). The capillary force due to the meniscus between the sample and tip is

$$F = 4\pi R\gamma \cos\theta/(1 + D/d), \tag{2}$$

where γ is the surface tension of the condensate and θ is the liquid-solid contact angle. d is the distance the tip extends into the meniscus and is given by $(\gamma V/RT)\cos\theta/\ln(P/P_s)$ where V is the condensate molar volume, R the gas constant, T the temperature, and P/P_s is the relative humidity (Israelachvili, 1991). For water, $\gamma = 0.073$ J/m^2 and $d = -(1.08\text{ nm})/\ln(P/P_s)$. Using these approximations, the spring constant $k_1 = -\partial F/\partial D$ is

$$k_1 = 4\pi R\gamma \cos\theta/d(1 + D/d)^2. \tag{3}$$

For relative humidities from 10% to 90%, k_1 ranges from about 12 to 15 N/m (Woodward and Zasadzinski, 1994). From an analysis of the meniscus profiles and interaction forces (Orr et al., 1975; Zasadzinski et al., 1987), the pressure within the fluid in the meniscus can exceed 100 atm, which is sufficient to damage soft materials, although it would only lead to small deformations of crystalline solids such as graphite (Mamin et al., 1986). The wide range of local pressures experienced by samples during scanning may explain the irreproducibility often found in imaging biological materials, especially those loosely adsorbed onto substrates and imaged in air.

We can estimate k_2, the spring constant between the sample and the STM base, for thin films. Replicas for both STM and TEM imaging are thin metal films mounted on porous metal mesh grids; where the replica is in direct contact with the mesh, k_2 is large. However, for the part of the replica that is loosely suspended over a pore of area a,

$$k_2 = ET^3/0.14(1 - \nu^2)a, \tag{4}$$

where E is the Young's modulus of the replica, ν is Poisson's ratio, and T is the thickness of the replica (Roark, 1965). Metal surface replicas prepared for TEM are about 25 nm thick, with $E \cong 2 \times 10^{10}$ N/m^2 and $\nu \cong 0.3$, and are mounted on a mesh with 30-μm spacings. Hence, $k_2 = 0.003$ N/m in the center of the mesh. Taken together with the estimate of k_1, Eq. 1 suggests a possible 1000-fold amplification, which is clearly outside the limits of our approximations but is also indicative of potential artifacts due to tip-sample interactions. Most importantly for reliable imaging, we cannot determine whether the particular area being imaged is supported well during a particular STM scan. Clearly, k_2 will vary significantly, depending on the relative location of the sample with respect to the support mesh. As a result, we expect, and have found, that feature heights often vary with location on the surface. This effect will not be appreciable for chemically and physically homogeneous "bulk" samples (>1 mm thick). However, even if the sample is "bulk," any weak point in the mounting or in the local adhesion of the sample to the substrate or the substrate to the STM base can lead to amplification of surface features. This also suggests that certain areas of a sample might be highly amplified, leading to permanent local distortion of the surface, where other areas might not be distorted at all. As controlling the properties of the sample surface is difficult, it is important to minimize these forces for reliable imaging.

It is clear that making the sample thicker and reducing the relative humidity are the best routes to minimizing sample height amplification. To control the environment and eliminate condensation between the tip and sample, and hence minimize k_1, the STM was enclosed in a bell jar with a base plate that allowed the evacuation of the chamber with a rotary pump to <0.1 torr. The chamber was then back-filled with dry nitrogen; because of the high voltages on the piezos, imaging at 0.1 torr pressure led to glow discharges and other problems (Woodward and Zasadzinski, 1994). To stiffen the replicas and to increase k_2, the platinum-carbon replicas for STM were sputter-coated with 0.2–0.5 μm of silver and the replicas were collected on silver wire filters with 0.2 μm nominal diameter pores. With these two modifications, feature heights measured by STM were reproducible for hours on a single sample (Woodward and Zasadzinski, 1994) and showed no variation with position on the replica.

Quantitative height measurements by correlation averaging

Just as in TEM, the resolution in any individual STM image of a freeze-fracture replica is limited by the granularity of the replicating film. In general, the quality of the replica is determined by how well the metal film replicates the surface on which it was deposited. However, the metal replicas are made up of small metal grains a few nanometers in diameter (Zasadzinski and Bailey, 1989; Ruben, 1989; Wepf et al., 1991; Woodward and Zasadzinski, 1996b). Because the surface energy of the metal layer is much higher than that of a fracture surface of water or hydrocarbon, the metal film does not spread or "wet" the surface, but aggregates into small droplets (Woodward and Zasadzinski, 1996b). The aggregates grow in size, eventually merging with neighboring aggregates to form a continuous conductive film. The grain is an inherent feature of the wetting properties of the sample and the replicating film and is the limiting factor in obtaining higher resolution images from either STM or TEM.

However, the grainy replicating film contributes a random noise component to the image that can be removed by proper image processing. Correlation averaging is often used in electron microscopy to enhance noisy images that contain a repeating pattern. Computer algorithms based on cross-correlation principles have been developed by several researchers (Frank et al., 1978; Crepeau and Fram, 1981; Saxton and Baumeister, 1982; Henderson et al., 1986) to locate and average patterns found in digitized images of electron micrographs. Averaging is widely used to

analyze images of biological structure with poor signal-to-noise ratios or those that do not form large crystal arrays. Following Schulz-DuBois and Rehberg (1981), we have used the structure function for correlation averaging when absolute pixel values are important. In its discrete form the structure function is

$$S(x', y') = \sum_{x=0}^{m-1} \sum_{y=0}^{m-1} [T(x, y) - M(x + x', y + y')]^2 \quad (5)$$

and is easy to recognize as the sum of the squared deviations between the test image $T(x, y)$ and the main image $M(x, y)$. For calculation by computer, the discrete form of the structure function (Eq. 5) is usually used in conjunction with the fast Fourier transform (FFT) algorithm. Here $T(x, y)$ is a $m \times m$ pixel test image, $M(x, y)$ is an $n \times n$ pixel main image, and x, x', y, and y' are all integers corresponding to the pixel location. The value of $T(x, y)$ or $M(x, y)$ is the digitized pixel intensity of the original image for electron micrographs or relative height values for scanning probe images. The coordinates (x', y') of the minima of the structure function $S(x', y')$ are taken to be the locations in the original image that most closely resemble the test image. By averaging over many of these areas, random noise is removed, giving a composite image that resembles the actual structure more closely than do any of the individual images. The dramatic improvement in image quality and resolution that results from correlation averaging often reveals structural information that is obscured in any individual image. Correlation averaging has only recently been applied to STM images (Soethout et al., 1988; Amrein et al., 1989; Stemmer et al., 1989; Wang et al., 1990; Woodward et al., 1995; Woodward and Zasadzinski, 1996a) and AFM images (Weigrabe et al., 1991), but its use in TEM is ubiquitous and its benefits are well established.

RESULTS

Representative TEM images of the 23°C and 16°C samples are shown in Fig. 1. In the 23°C and 20°C samples, the ripples are continuous and the ripple asymmetry is apparent from the variation in shadowing across the image (Zasadzinski and Schneider, 1987). Near the open arrow, the ripples appear as wider light gray lines with narrow, dark gray lines. At the filled arrow, the pattern is reversed—narrow light gray lines with wide, dark gray lines. These patterns are consistent with an asymmetrical waveform for the ripples; the shadow patterns change abruptly near the center of the image, indicating a boundary between domains of different orientation (Zasadzinski and Schneider, 1987). In TEM images of the 18°C and 16°C samples, the ripples are discontinuous and appear to be made up of a line of beads. This pattern of beads is consistent with a self-shadowing artifact; the oblique metal deposition enhances small features in the fracture surface (Ruben, 1989). It is clear that the ripple is of smaller amplitude, and the shadowing pattern has lost its asymmetry and is less well defined, suggesting a temperature dependence of the ripple amplitude. When the replica is made by depositing the metal film normal to the surface (which eliminates self-shadowing), TEM images of the 18 and 16°C samples are featureless. The wavelength of the ripples is 11.0 ± 1.0 nm for all four temperatures. The measured values for the wavelength are in good agreement with the value of 11–12 nm found by x-ray diffraction (Janiak et al., 1979; Wack and Webb, 1989) or freeze-fracture TEM of DMPC (Luna and McConnell, 1977; Ruppel and Sackmann, 1983; Zasadzinski and Schneider, 1987).

Survey STM scans of the 23°C and the 20°C samples show that the STM and TEM images have the same defect patterns and general features (Fig. 2 *a–c*). The gray scale in

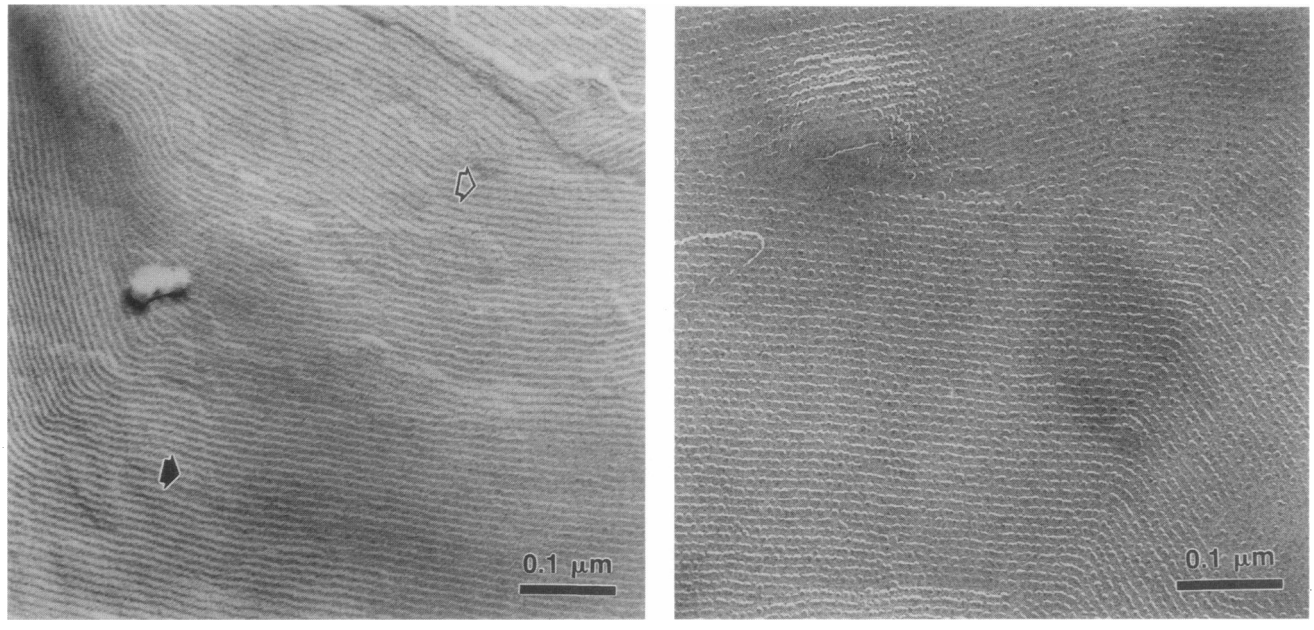

FIGURE 1 (*a*) TEM image of DMPC in excess water at 23°C. The ripples change orientation over micron length scales, typically at 120° angles, indicating an underlying hexagonal packing. The ripple asymmetry can be inferred from the shadow patterns: narrow dark gray/wide light gray lines in the upper right of the image (*open arrow*) adjacent to narrow light gray/wide dark gray lines in the lower left of the image (*filled arrow*). (*b*) TEM image of DMPC in excess water at 16°C (the sample at 18°C was similar). The ripples are much less well defined and appear like a string of beads. This beading is induced by a self-shadowing process that enhances small features. The ripple amplitude is much smaller and the asymmetry in the shadowing has disappeared. Replicas made by vertical shadowing to eliminate the self-shadowing artifact showed no periodicities.

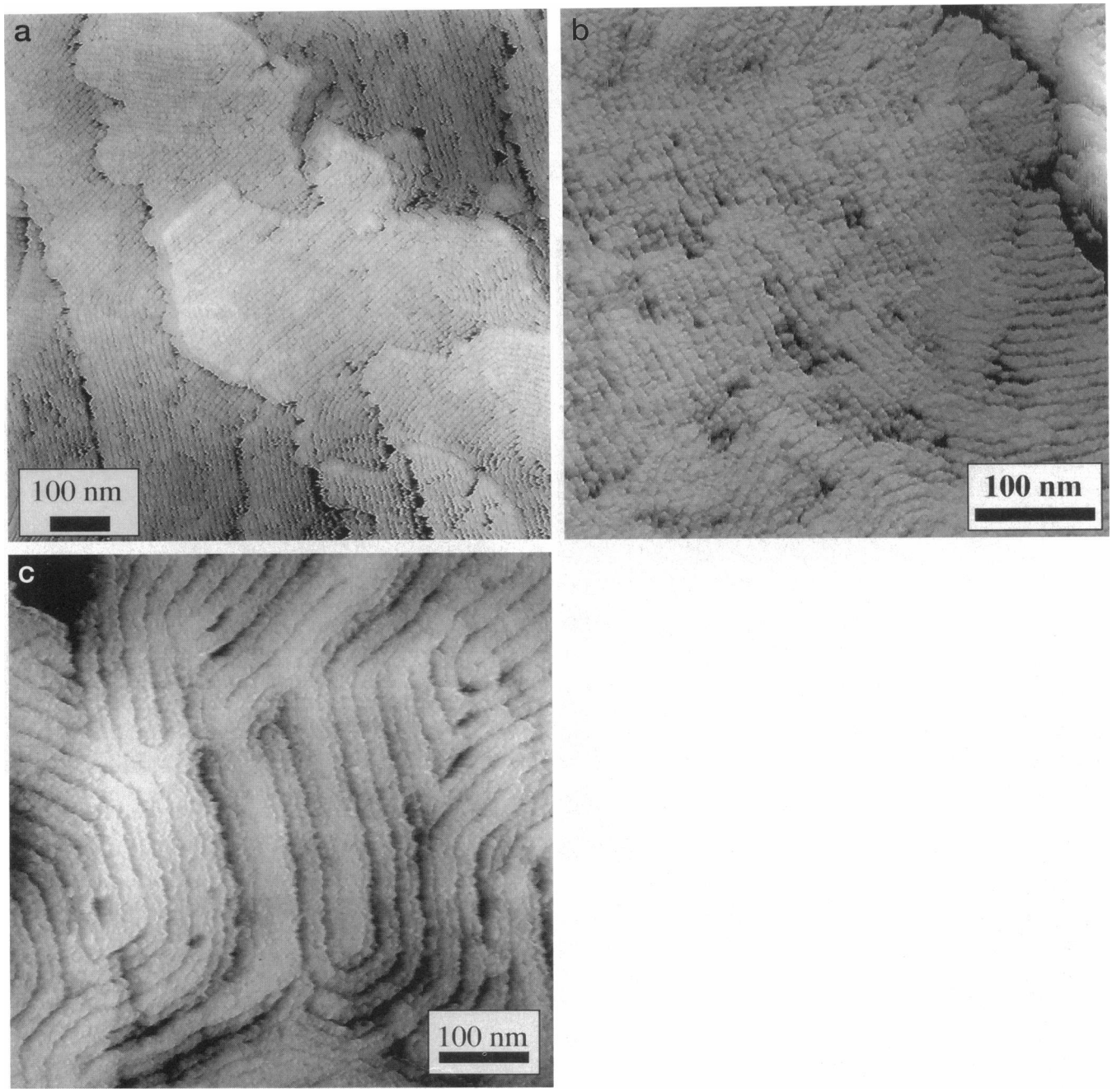

FIGURE 2 (*a*) Low-resolution STM image of replica of DMPC ripples to compare to the TEM images in Fig. 1 *a*. The general pattern of ripples is very similar to the TEM images. Note especially that the ripples appear to be very uniform in height over various patches on the surface, each of which is separated by a bilayer thickness. The threefold symmetry of the ripple orientations is preserved over many microns, indicating long-range molecular ordering. (*b*) Intermediate-resolution STM image of DMPC ripples showing area typically used for image analysis. The ripples are uniformly oriented over a large distance and are relatively defect free. The granularity of the replicating film is becoming apparent at this magnification. (*c*) Second type of ripple often observed in DMPC replicas. These ripples are significantly larger in amplitude and about twice the wavelength of the majority ripples shown in *a* and *b*. These ripples appear to have an inverted W shape and have a larger amplitude than the first type of ripple.

each domain of the ripple texture is quite uniform in Fig. 2 *a*, indicating a consistent ripple height—adjacent domains are also of uniform gray scale and are likely to be separated by a bilayer step, as is generally observed in TEM images. The threefold symmetry of the ripple phase and the long-range orientational order of the ripples is also consistent with the TEM images (Fig. 2 *b*) and suggests that the underlying hexagonal molecular ordering is long range (Fig. 1) (Zasadzinski and Schneider, 1987). Fig. 2 *c* shows a region dominated by the larger wavelength, symmetrical ripples, often called the λ ripples (Ruppel and Sackman, 1983). These have a wavelength of about 20 nm and the shape of an inverted W. The λ ripples were relatively rare and generally did not present large, oriented domains, so a

detailed analysis of their shape and amplitude was not attempted.

To quantify the ripple amplitude and wavelength, 20 250 × 250 nm STM images with the ripples oriented in a single direction were analyzed for each sample to quantify the ripple features observed by TEM. Several different STM tips were used on each sample to eliminate any possible asymmetries or artifacts associated with a given tip. At this image size, each ripple has about 20 pixels per wavelength (images are 512 × 512 pixels). Twenty pixels are sufficient to accurately describe the ripple configuration without oversampling. Fig. 3, *a* and *b*, contains representative images from the 23°C sample, and Fig. 3 *c* is representative of the 20°C samples. Samples prepared at 18°C and 16°C showed

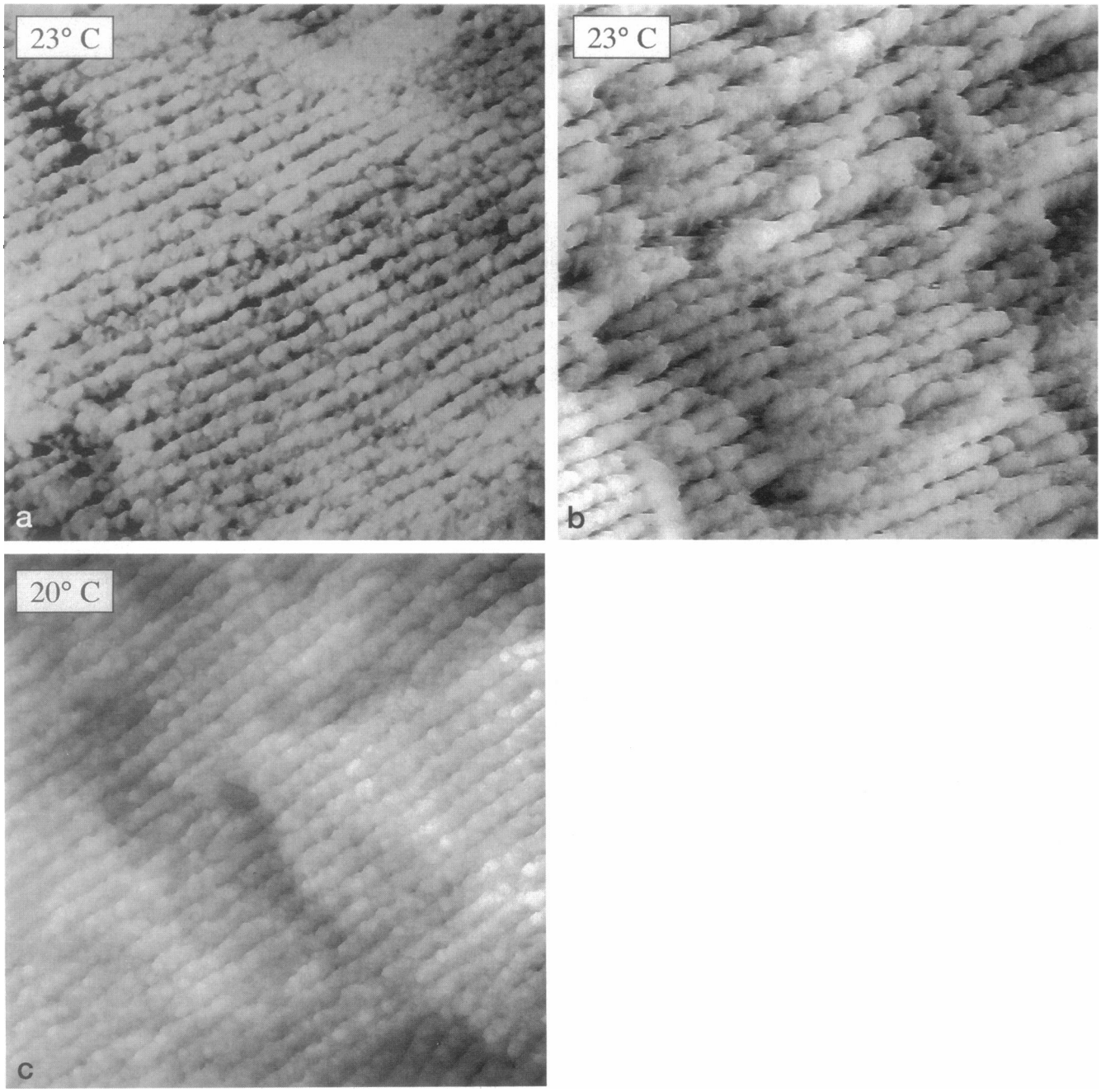

FIGURE 3 (*a*) 250 nm × 250 nm STM image of a freeze-fracture replica of DMPC in excess water originally at 23°C. The ripple shape is obscured by the finite size of the metal grains that make up the replica film, imperfections in the ripples themselves, and noise from the STM. Correlation averaging helps eliminate these features to enhance the image quality. The raw images were not processed, to ensure the fidelity of the height information. (*b*) 250 × 250 nm STM image of a different replica of DMPC in excess water originally at 23°C. This image shows the variation in morphology we observed between samples. The general features of the ripples and the amplitudes were quite consistent between samples and STM tips and imaging conditions, as can be seen from Table 1. (*c*) 250 nm × 250 nm STM image of a freeze-fracture replica of DMPC in excess water originally at 20°C. The apparent amplitude of the ripples has decreased as compared with Fig. 4 *a*.

no modulated textures. Fourier transforms of both the smaller and larger scale images were used to evaluate the ripple wavelength, which was consistent with the TEM results (see Table 1). The grain of the Pt/C replica is obvious in these high-magnification images and obscures the details of the ripple shape, although the regular undulations of the replica are equally obvious from the images. The ripple amplitude appears smaller in the 20°C image (Fig. 3 *c*) than the 23°C images (Fig. 3 *a* and *b*). STM images suitable for analysis were averaged using the structure function program described earlier on a Silicon Graphics Indigo computer. A test area size of 32 × 32 pixels was used to ensure that the test area contained at least one complete ripple. Areas that showed a minimum square deviation from the test image were then averaged to make a composite image (Woodward and Zasadzinski, 1994). The composite image was then used as the test image to determine a new composite and eliminate any bias in the original choice of test image. Fig. 3, *a* and *b*, shows the variation between STM images of different samples frozen from the same 23°C temperature. Typically, 1000–4000 areas were used to make a composite. For any given image we determined four different composites using four different test areas chosen arbitrarily from the original image. There was no difference in the composites that came from the different initial test areas. In addition to averaging out any effects of the metal grains, the correlation analysis removes any bias of the observer as to the best ripple shape.

TABLE 1 Amplitude of first two harmonics and wavelength of ripples from different images as determined by correlation averaging

Temperature	A_1 (nm)	A_2 (nm)	λ (nm)
20°C	0.62	0.12	10.2
	0.64	0.16	10.4
	0.44	0.07	10.2
	0.42	0.06	10.1
	0.44	0.06	10.3
	0.45	0.07	10.3
	0.64	0.10	12.9
23°C	1.20	0.25	10.9
	1.05	0.20	11.4
	1.03	0.20	10.8
	0.96	0.20	10.3
	1.02	0.20	11.2
	1.72	0.36	11.0
	1.82	0.38	11.0
	1.29	0.36	10.9
	0.98	0.26	10.9
	0.68	0.21	10.1
	0.54	0.16	9.8
	0.86	0.20	10.0
	1.16	0.28	10.5
	0.98	0.27	10.5
	1.03	0.30	10.3
	0.95	0.34	11.0
	1.08	0.40	11.0
	1.18	0.40	11.0
	0.74	0.14	10.4
	1.34	0.30	10.1
	1.19	0.25	10.1

The average ripple conformation determined from the composite image was then fit to a sum of harmonics using the nonlinear least-squares fitting routine found in C-PLOT (Cambridge, MA) to eliminate any systematic errors introduced by specific samples, images, STM tips, etc. The parameters fit were the amplitudes and phases of the first three harmonics of a sine wave, and the wavelength of the ripple. The data for both sets of samples are presented in Table 1. The average values of the first two harmonics for the 23°C samples are 1.1 ± 0.3 nm and 0.3 ± 0.1 nm, and the averaged wavelength is 10.7 ± 1.0 nm. For the 20°C samples, the amplitude of the first harmonic is 0.5 ± 0.2 nm, the second amplitude is 0.1 ± 0.1 nm, and the wavelength is 10.6 ± 1.0 nm. The amplitude of the third harmonic was negligible for both temperatures. The presence of a nonzero amplitude of the second harmonic shows that the ripples are asymmetrical, as expected from the TEM micrographs. Fig. 4 shows a cross section of the ripple conformation calculated from the average values. The fits give a peak-to-valley height of 2.4 nm for the ripple at 23°C and 1.1 nm at 20°C. Combined with the zero amplitude we found at 18°C and 16°C, this shows a distinct temperature dependence of the ripple amplitude in the $P_{\beta'}$ phase. The wavelength of the ripples was independent of temperature within our experimental error.

In our previous STM images of ripples, filtered images showed a significantly different amplitude of about 4.5 nm. From the earlier discussion, this significantly larger amplitude most likely was due to amplification caused by imaging in air; the actual number of images measured was also very small—only two images were measured. The large number of samples and the extensive correlation averaging used here provide a much better estimate of the ripple amplitude and waveform and provide a realistic error limit

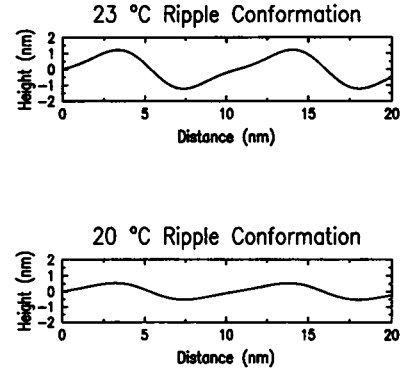

FIGURE 4 (*a*) Average ripple cross section at 23°C, as determined from the average of the parameters in Table 1. The wavelength is 10.7 ± 1 nm, and the peak-to-valley amplitude is 2.4 nm. (*b*) Average ripple cross section at 20°C. The wavelength is 10.6 ± 1 nm, and the peak-to-valley height decreases to 1.1 nm. The asymmetry in the waveform is still present. Samples quenched from 18°C and 16°C showed no apparent modulation, indicating that their amplitude was less than 0.5 nm.

on our results. Our earlier work also showed what looked like a small secondary ripple perpendicular to the primary ripple (Zasadzinski et al., 1988). Subsequent x-ray results have suggested that this secondary ripple may be the result of molecular tilt perpendicular to the ripple wavevector (Hentschel and Rustichelli, 1991). However, Fourier transforms of our STM and TEM images do not have any peaks other than those of the primary ripple. This secondary ripple and the larger amplitudes are likely artifacts caused by the height amplification discussed earlier, as those images were taken in air. As an additional check for the secondary ripple, we looked at autocorrelations of the STM images and found no periodicity perpendicular to the primary ripple. Fig. 5, *a* and *b*, shows the autocorrelation and cross sections from the images shown in Fig. 3, *a* and *c*, respectively. These show that the ripple is uniaxial over the length scale of the images.

DISCUSSION

Our combined STM and TEM results show that in excess water, bilayers of DMPC have uniaxial, asymmetrical ripples with a temperature-dependent amplitude, varying from 2.4 nm peak-to-peak near the chain-melting temperature to near zero near the chain crystallization temperature. It is difficult to say whether the STM tip can actually reach the bottom of each trough of every ripple during a particular scan; the reproducibility of the data between different samples and different tips suggests that any errors introduced are minimal. The ripple wavelength of 11 nm does not change with temperature. The variance of our data reported in Table 1 gives a reasonable estimate of the precision of these results; the variances in the ripple wavelength are not significantly larger than those reported by Wack and Webb

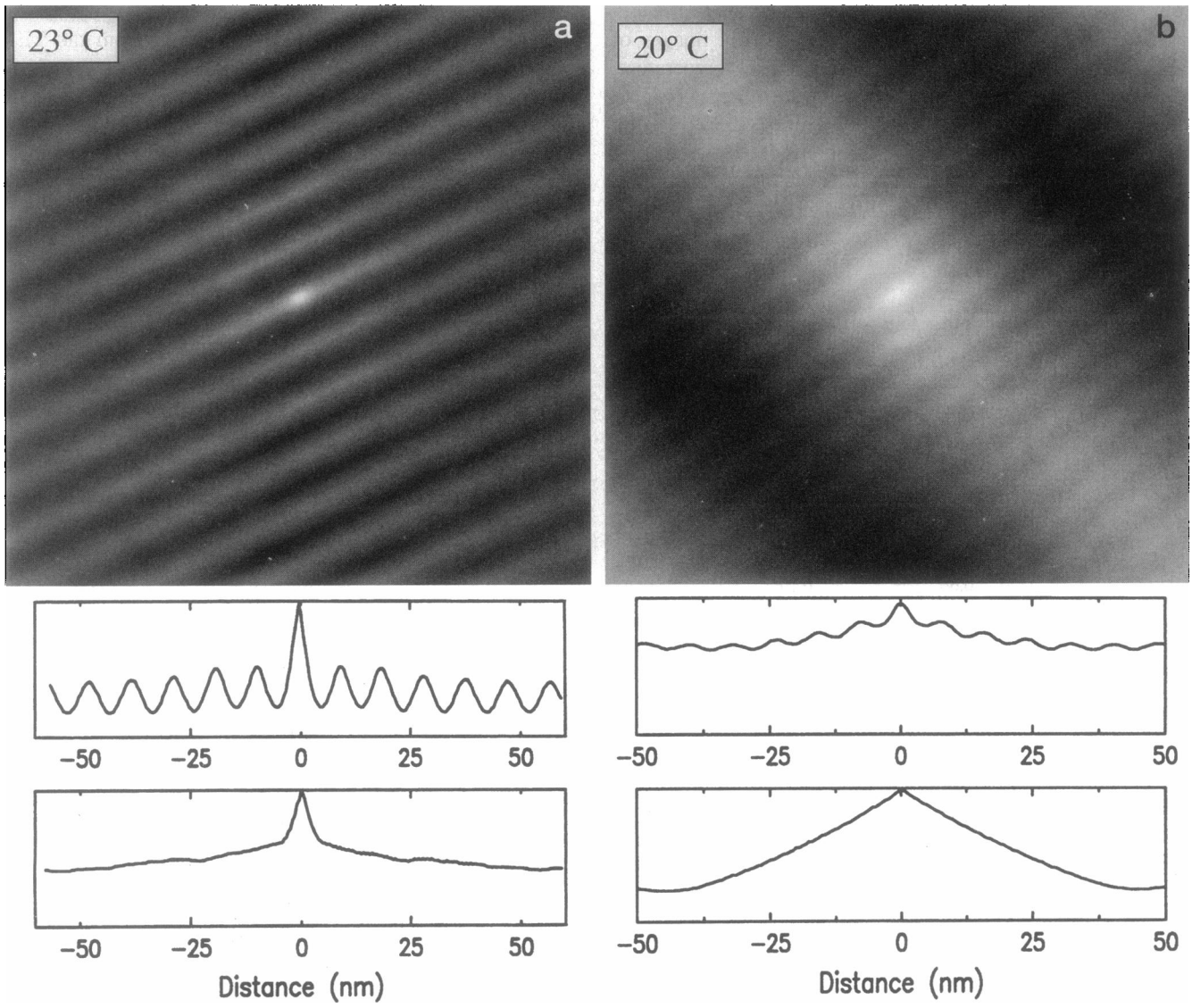

FIGURE 5 (*a*) Autocorrelation of the sample quenched from 23°C shown in Fig. 3 *a* and cross sections along (*top*) and perpendicular to (*bottom*) the ripple direction. The lack of modulation perpendicular to the ripple direction rules out any significant secondary modulation (Zasadzinski et al., 1988). (*b*) Autocorrelation of the sample quenched from 20°C shown in Fig. 3 *c* and cross sections along (*top*) and perpendicular to (*bottom*) the ripple direction. The ripple structure is uniaxial at all temperatures investigated.

(1989) using synchotron x-ray diffraction. These results are also consistent with those of Sun et al. (1996), who determined a ripple amplitude of 1.9 nm for DMPC with 25% water via a detailed model fitting of Wack and Webb's x-ray data (1989). (At the higher water fractions used here, the available x-ray diffraction data were not sufficiently detailed to provide an equal level of model fitting.) The ripple wavelength invariance with temperature is also consistent with neutron (Mortensen et al., 1988) and x-ray diffraction results (Matuoka et al., 1994). The data of Mortensen et al. (1988) also showed that the absolute scattered intensity from the ripples increased with increasing temperature, which is consistent with an increasing ripple amplitude with increasing temperature. The close agreement found between x-ray, neutron, and our STM data gives strong support to our basic assumption that the freezing and replication steps did not alter the basic structure of the ripple.

Our finding of a second harmonic in the ripple profile confirms that the ripple is indeed asymmetrical. The asymmetrical ripple shape is consistent with freeze-fracture electron microscopy (Zasadzinski and Schneider, 1987), x-ray diffraction (Katsaras and Raghunathan, 1995; Sun et al., 1996), and a recent theory (Lubensky and MacKintosh, 1993) that suggests the ripple is the result of a coupling between molecular tilt and bilayer bending. The theory depends, to some extent, on the chiral nature of DMPC, although experimental results show that the ripple is unchanged when a racemic mixture of DMPC is used (Zasadzinski, 1988; Katsaras and Raghunathan, 1995). However, the temperature dependence of the ripple amplitude, which is significantly larger than our error estimates, has not previously been observed experimentally or been predicted theoretically. However, it is not unexpected, as the bend elasticity of the membrane decreases dramatically over the transition from crystalline to fluid bilayers as the temperature is raised through the $P_{\beta'}$ phase. The softer bilayer would be expected to buckle with an increasing amplitude, as is observed. Both STM and TEM show that the wavelength of the ripples is unchanged at all four temperatures. This indicates that models of the ripple phase based on a fixed offset of neighboring molecules due to packing frustration must be modified (Schwartz et al., 1994). Such theories predict that the wavelength of the ripple would scale with the amplitude, in contradiction to our results. However, a change in molecular tilt with temperature might change the vertical component of a fixed molecular offset as the temperature increases from the tilted $L_{\beta'}$ phase to the untilted L_α phase. We have also carefully investigated the possibility of a second modulation normal to the first set of ripples by examining autocorrelations of the ripple images. No secondary ripple structure was found, indicating that 1) the ripples are uniaxial, 2) previous indications of such ripples were likely artifacts (Zasadzinski et al., 1988), and 3) they were not related to a change in hydrocarbon tilt direction (Hentschel and Rustichelli, 1991).

This modified freeze-fracture technique can extend the utility of STM to imaging bulk suspension, liquid crystals, and other biological materials in excess water. The technique is substrate-free and can examine interior interfaces impossible to see with other scanned probe microscopies at high resolution. The quantitative, three-dimensional information available by this technique is a necessary extension of TEM images of replicas, especially for situations in which a repetitive, three-dimensional structure is expected and quantitative information about the third (or vertical) dimension is needed. By incorporating the necessary modifications, replicas for STM can be made as easily as those for TEM with no additional investment. We have found that it is necessary to do our STM imaging of these replica surfaces in as dry an atmosphere as possible to inhibit amplification of surface features. This is an important caveat to any STM or AFM imaging done in ambient conditions. However, images of the STM replicas are reproducible and simple to interpret once these precautions are taken. On any particular replica, the granularity of the replica film limits resolution to about 2 nm laterally and about 1 nm vertically. However, the effects of the granularity can be removed by correlation averaging using a structure function to preserve absolute height information, especially for periodic surfaces. The ultimate resolution of the technique for the ripple phase of phospholipids is <1 nm laterally and 0.3 nm vertically, as estimated from the error in our measurements. The replica/STM technique offers a higher resolution than most direct STM or AFM imaging of supported biological materials and is easier to interpret and reproduce. It can also be used as a check for tapping mode AFM images of soft surfaces and is the only truly substrate-free method available for imaging biomembrane liposomes and other materials.

We thank R. Viswanathan for preparing Langmuir-Blodgett films and L. Madsen for help with correlation averaging.

This work was supported by National Institutes of Health grant HL51177 and made use of MRL Central Facilities under NSF award DMR-9123048.

REFERENCES

Adamson, A. W. 1990. The Physical Chemistry of Surfaces. John Wiley and Sons, New York. Ch. 4, pp. 106–118.

Amrein, M., R. Durr, H. Winkler, G. Travaglini, R. Wepf, and H. Gross. 1989. STM of freeze dried and Pt-Ir-C-coated bacteriophage-T4 polyheads. *J. Ultrastruct. Mol. Struct. Res.* 102:170–177.

Amrein, M., A. Stasiak, H. Gross, E. Stoll, and G. Travaglini. 1988. Scanning tunneling microscopy of recA-DNA complexes coated with a conducting film. *Science.* 240:514–516.

Anselmetti, D., Ch. Gerber, B. Michel, H. Wolf, H. J. Guntherodt, and J. Rohrer. 1993. Deformation-free topography from combined scanning force and tunneling experiments. *Europhys. Lett.* 23:421–426.

Arca, M., A. J. Bard, B. R. Horrocks, T. C. Richards, and D. A. Treichel. 1994. Advances in scanning electrochemical microscopy. *Analyst.* 119: 719–726.

Bailey, S. M., M. L. Longo, S. Chiruvolu, and J. A. Zasadzinski. 1991. A controlled temperature and environmental stage for rapid freezing fixation for freeze fracture. *J. Electron. Microsc. Tech.* 19:118–126.

Bailey, S. M., and J. A. Zasadzinski. 1991. Validation of convection limited cooling of samples for electron microscopy. *J. Microsc.* 163: 307–320.

Bellare, J., H. T. Davis, L. E. Scriven, and Y. Talmon. 1988. The controlled environment vitrification system. *J. Electron Microsc. Tech.* 10:87–104.

Binnig, G., C. F. Quate, and Ch. Gerber. 1986. Atomic force microscope. *Phys. Rev. Lett.* 56:930–933.

Binnig, G., H. Rohrer, Ch. Gerber, and E. Weibel. 1982. Surface studies by scanning tunneling microscopy. *Phys. Rev. Lett.* 49:57–61.5.

Blackman, G. S., C. M. Mate, and M. R. Philpott. 1990. Interaction forces of a sharp tungsten tip with molecular films of silicon surfaces. *Phys. Rev. Lett.* 65:2270–2273.

Branton, D. 1966. Fracture faces of frozen membranes. *Proc. Natl. Acad. Sci. USA.* 55:1048–1056.

Carlson, J. M., and J. P. Sethna. 1987. Theory of the ripple phase in hydrated phospholipid bilayers. *Phys. Rev. A.* 36:3359–3374.

Cevc, G. 1991. Polymorphism of the bilayer membranes in the ordered phase and the molecular origin of th elipid pretransition and rippled lamellae. *Biochem. Biophys. Acta.* 1062:59–69.

Chen, C. J. 1992. Effects of $m \neq 0$ tip states in STM: the explanation of corrugation reversal. *Phys. Rev. Lett.* 69:1656–1659.

Chiruvolu, S., E. Naranjo, and J. A. Zasadzinski. 1994. Microstructure of complex fluids by electron microscopy. *In* ACS Symposium Series, Vol. 578, Structure and Flow in Surfactant Solutions. C. A. Herb and R. K. Prud'homme, editors. American Chemical Society, Washington, DC., pp. 86–104.

Ciraci, S., A. Baratoff, and I. P. Batra. 1990. Tip-sample interaction effects in scanning tunneling and atomic force microscopy. *Phys. Rev. B.* 41:2763–2775.

Clemmer, C. R., and T. P. Beebe. 1991. Graphite—a mimic for DNA and other biomolecules in scanning tunneling microscope studies. *Science.* 251:640–642.

Clemmer, C. R., T. P. Beebe, S. M. Lindsay, K. W. Hipps, M. Amrein, and H. Gross. 1992. A review of graphtie and gold surface studies for use as substrates in biological scanning tunneling microscopy studies. *Scanning Microsc.* 6:319–333.

Costello, M. J., S. Meiboom, and M. J. Sammon. 1984. Electron microscopy of a cholesteric liquid crystal and its blue phase. *Phys. Rev. A.* 29:2957–2959.

Crepeau, R. H., and E. K. Fram. 1981. Reconstruction of imperfectly ordered zinc-induced tubulin sheets using cross-correlation and real space averaging. *Ultramicroscopy.* 6:7–18.

Derjaguin, B. V., Y. I. Rabinovich, and N. V. Churaev. 1978. Direct measurement of molecular forces. *Nature.* 272:313–318.

Doniach, S. 1979. A thermodynamic model for the monoclinic (ripple) phase of hydrated phospholipid bilayers. *J. Chem. Phys.* 70:4587–4596.

Erlandsson, R., S. Chiang, C. M. Mate, and G. M. McClelland. 1988. Atomic force microscopy using optical interferometry. *J. Vac. Sci. Technol. A.* 6:266–270.

Fetter, R. D., and M. J. Costello. 1985. A procedure for obtaining complementary replicas of ultra-rapidly frozen sandwich samples. *J. Microsc.* 141:277–290.

Florin, E-L., V. T. Moy, and H. E. Gaub. 1994. Adhesion forces between individual ligand-receptor pairs. *Science.* 264:415–418.

Foster, J. S., and J. E. Frommer. 1988. Imaging liquid crystals using a tunneling microscope. *Nature.* 333:542–545.

Foster, J., J. E. Frommer, and P. C. Arnett. 1988. Molecular manipulation using a tunneling microscope. *Nature.* 331:324–326.

Frank, J., W. Goldfarb, D. Eisenberg, and T. S. Baker. 1978. Reconstruction of glutamine synthetase using computer averaging. *Ultramicroscopy.* 3:283–290.

Frisbie, C. D., L. F. Rozsnyai, A. Noy, M. S. Wrighton, and C. M. Lieber. 1994. Functional group imaging by chemical force microscopy. *Science.* 265:2071–2074.

Garnaes, J. D., K. Schwartz, R. Viswanathan, and J. A. Zasadzinski. 1993. Nanoscale defects in Langmuir-Blodgett films observed by atomic force microscopy. *J. Synthetic Metals.* 55:3975–3800.

Goldstein, R. E., and S. Leibler. 1988. Model for lamellar phases of interacting lipid membranes. *Phys. Rev. Lett.* 61:2213–2216.

Gould, S., O. Marti, B. Drake, L. Hellemans, C. E. Bracker, P. K. Hansma, N. L. Keder, M. M. Eddy, and G. D. Stuckey. 1988. Molecular resolution images of amino acid crystals with the atomic force microscope. *Nature.* 332:332–334.

Guckenberger, R., M. Heim, G. Cevc, H. F. Knapp, W. Wiegrabe, and A. Hillebrand. 1994. Scanning tunneling microscopy of insulators, and biological specimens based on lateral conductivity of ultrathin water films. *Science.* 266:1538–1540.

Gulik-Krzywicki, T., and M. J. Costello. 1978. Use of low temperature x-ray diffraction to evaluate freezing methods used in freeze-fracture electron microscopy. *J. Microsc.* 112:102–113.

Hallmark, V. M., S. Chiang, J. F. Rabolt, J. D. Swalen, and R. D. Wilson. 1987. Observation of atomic organization on Au (111) by STM. *Phys. Rev. Lett.* 59:2879–2882.

Hansma, P. K., J. B. Cleveland, M. Radmacher, D. A. Walters, P. E. Hillner, M. Bezanilla, M. Fritz, D. Vie, H. G. Hansma, C. B. Prater, J. Massie, L. Fukunaga, J. Gurley, and V. Elings. 1994. Tapping mode AFM in liquids. *Appl. Phys. Lett.* 64:1730–1740.

Hansma, P. K., V. B. Elings, O. Marti, and C. E. Bracker. 1988. Scanning tunneling microscopy and atomic force microscopy: some applications to biology and technology. *Science.* 242:209–216.

Hansma, P. K., and J. Tersoff. 1987. Scanning tunneling microscopy. *J. Appl. Phys.* 61:R1–R23.

Hatta, I., S. Kato, and H. Takahashi. 1993. Phase transitions and polymorphism in phospholipids. *Phase Transitions.* 45:157–184.

Hegerl, R. 1992. A brief survey of software packages for image processing in biological electron microscopy. *Ultramicroscopy.* 46:417–423.

Henderson, R., J. M. Baldwin, K. H. Downing, J. Lepault, and F. Zemlin. 1986. Structure of purple membrane from halobacterium halobium: recording, measurement and evaluation of electron micrographs at 3.5 Å resolution. *Ultramicroscopy.* 19:147–178.

Hentschel, M. P., and F. Rustichelli. 1991. Structure of the ripple phase in hydrated phosphatidylcholine multimembranes. *Phys. Rev. Lett.* 66: 903–906.

Hörber, J. K. H., C. A. Lang, T. W. Hänsch, W. M. Heckl, and H. Möhwald. 1988. Scanning tunneling microscopy of lipid films and embedded molecules. *Chem. Phys. Lett.* 145:151–158.

Hui, S. W., R. Viswanathan, J. A. Zasadzinski, and J. Israelachvili. 1995. The structure and stability of phospholipid bilayers by atomic force microscopy. *Biophys. J.* 68:171–178.

Ihn, K. J., J. A. Zasadzinski, R. Pindak, A. J. Slaney, and J. Goodby. 1992. Freeze-fracture TEM observations of the liquid crystal analog of the Abrikosov phase. *Science.* 258:275–278.

Israelachvili, J. N. 1991. Intermolecular and Surface Forces. Academic Press, London. 177, 330–332.

Jacobson, K., E. D. Sheets, and R. Simson. 1995. Revisiting the fluid mosaic model of membranes. *Science.* 268:1441–1442.

Jahn, W., and R. Strey. 1988. Microstructure of microemulsions by freeze-fracture electron microscopy. *J. Phys. Chem.* 92:2294–2301.

Janiak, M. J., D. M. Small, and G. G. Shipley. 1979. Temperature and compositional dependence of the structure of hydrated dimyristoyl lecithin. *J. Biol. Chem.* 254:6068–6078.

Katsaras, J., and V. A. Raghunathan. 1995. Molecular chirality and the "ripple" phase of phosphatidylcholine multibilayers. *Phys. Rev. Lett.* 74:2022–2025.

Keller, S. L., S. M. Bezrukov, S. M. Gruner, M. W. Tate, I. Vodyanoy, and V. A. Parsegian. 1993. *Biophys. J.* 65:23–27.

Kleman, M., C. E. Williams, M. J. Costello, and T. Gulik-Kryzwicki. 1977. Defect structures in lyotropic phases revealed by freeze-fracture electron microscopy. *Phil. Mag.* 35:33–56.

Krbecek, R., C. Gebhardt, G. Gruler, and E. Sackmann. 1979. Three-dimensional microscopic surface profiles of membranes reconstructed from freeze-etching electron micrographs. *Biochim. Biophys. Acta.* 554:1.

Lang, C. A., J. K. H. Hörber, T. W. Hänsch, W. M. Heckl, and H. Möhwald. 1988. Scanning tunneling microscopy of Langmuir-Blodgett films on graphite. *J. Vac. Sci. Technol. A.* 6:368–370.

Lindsay, S. M., and B. Barris. 1988. Imaging deoxyribose nucleic acid molecules on a metal surface under water by scanning tunneling microscopy. *J. Vac. Sci. Technol. A.* 6:544–547.

Longo, M. L., A. M. Bisagno, J. A. Zasadzinski, R. Bruni, and A. J. Waring. 1993. A function of lung surfactant protein SP-B. *Science.* 261:453–456.

Lubensky, T. C., and F. C. MacKintosh. 1993. Theory of "ripple" phases of lipid bilayers. *Phys. Rev. Lett.* 71:1565–1568.

Luna, E. J., and H. M. McConnell. 1977. The intermediate monoclinic phase of phosphatidylcholines. *Biochim. Biophys. Acta.* 466:381–392.

Mamin, H., G. E. Ganz, D. W. Abraham, R. E. Thompson, and J. Clarke. 1986. Contamination mediated deformation of graphite by the STM. *Phys. Rev. B.* 34:9015–9018.

Manne, S., J. P. Cleveland, H. E. Gaub, G. D. Stucky, and P. K. Hansma. 1994. Direct visualization of surfactant hemimicelles by force microscopy of the electrical double layer. *Langmuir.* 10:4409–4413.

Matuoka, S., S. Kato, and I. Hatta. 1994. Temperature change of the ripple structure in fully hydrated DMPC/cholesterol multilayers. *Biophys. J.* 67:728–736.

McCullough, W. S., and H. L. Scott. 1990. Statistical-mechanical theory of the ripple phase of lipid bilayers. *Phys. Rev. Lett.* 65:931–934.

Meyer, E., R. Overney, D. Brodbeck, L. Howald, and J. Frommer. 1992. Friction and wear of Langmuir-Blodgett films observed by friction force microscopy. *Phys. Rev. Lett.* 69:1777–1780.

Mortensen, K., W. Pfeiffer, E. Sackmann, and W. Knoll. 1988. Structural properties of a phsophatidylcholine-cholesterol system as studied by small angle neutron scattering: ripple structure and phase diagram. *Biochim. Biophys. Acta.* 945:221–245.

Mou, J., J. Yang, and Z. Shao. 1994. Tris(hydroxymethyl)aminomethane induced ripple phase in supported unilamellar phospholipid bilayers. *Biochemistry.* 33:4349–4443.

Muller-Reichert, T., H. J. Butt, and H. Gross. 1996. STM of metal embedded and coated DNA and DNA-protein complexes. *J. Microsc.* 182:169–176.

Nagle, J. F., R. Zhang, S. Tristam-Nagle, W. Sun, H. Petrache, and R. M. Suter. 1996. X-ray structure determination of fully hydrated L_α phase DPPC bilayers. *Biophys. J.* 70:1419–1431.

Niblack, W. 1986. An Introduction to Digital Image Processing. Prentice-Hall International, Englewood Cliffs, NJ. 106–110.

Obcemea, C. H., and B. Vidic. 1992. Bilipid layer molecular organization in $P_{\beta'}$ phase studied by scanning tunneling microscopy. *Ultramicroscopy.* 42–44:1019–1024.

Orr, F. M., L. E. Scriven, and A. P. Rivas. 1975. Pendular rings between solids: meniscus properties and capillary force. *J. Fluid Mech.* 67: 723–742.

Overney, R. M., E. Meyer, J. Frommer, J., D. Brodbeck, and L. Howald. 1992. Friction measurements on phase separated thin films with a modified atomic force microscope. *Nature.* 359:133–135.

Patrick, D. L., and Beebe, T. P. 1993. On the origin of large scale periodicities observed during scanning tunneling microscopy studies of highly ordered pyrolytic graphite. *Surface Sci.* 297:L119–L121.

Quate, C. F. 1986. Vacuum tunneling: a new technique for microscopy. *Phys. Today.* 39:26–33.

Radmacher, M., M. Fritz, H. G. Hansma, and P. K. Hansma. 1994. Direct observation of enzyme activity with the atomic force microscope. *Science.* 265:1577–1579.

Roark, R. J. 1965. Formulas for Stress and Strain. McGraw-Hill, New York. 225.

Ruben, G. C. 1989. Ultrathin vertically shadowed platinum-carbon replicas for imaging individual molecules in freeze-etched biological DNA and material science metal and plastic specimens. *J. Electron Microsc. Tech.* 13:335–354.

Ruppel, D., and E. Sackman. 1983. On the defects in different phases of two-dimensional lipid bilayers. *J. Phys. (France).* 44:1025–1034.

Sammon, M. J., J. A. Zasadzinski, and M. R. Kuzma. 1987. Electron microscope observation of the nematic-smectic transition in a lyotropic liquid crystal. *Phys. Rev. Lett.* 57:2834–2837.

Saxton, W. O., and W. Baumeister. 1982. The correlation averaging of a regularly arranged bacterial cell envelope protein. *J. Microsc.* 127: 127–138.

Schneider, M. B., W. K. Chan, and W. W. Webb. 1983. Fast diffusion along defects and corrugations in phospholipid $P_{\beta'}$ liquid crystals. *Biophys. J.* 43:157–165.

Schulz-DuBois, E. O., and I. Rehberg. 1981. Structure function in lieu of correlation function. *Appl. Phys.* 24:323–329.

Schwartz, D. K., R. Viswanathan, J. Garnaes, and J. A. Zasadzinski. 1992a. Surface order and stability of Langmuir-Blodgett films. *Science.* 257: 508–511.

Schwartz, D. K., R. Viswanathan, and J. A. Zasadzinski. 1992b. Reorganization and crystallite formation in Langmuir-Blodgett films. *J. Phys. Chem.* 96:10444–10447.

Schwartz, D. K., R. Viswanathan, and J. A. Zasadzinski. 1994. Head-tail competition and modulated structures in planar surfactant (Langmuir-Blodgett) films. *J. Chem. Phys.* 101:7161–7168.

Scott, H. L., and McCullough. 1991. Theories of the modulated "ripple" phase of lipid bilayers. *Int. J. Modern Phys.* 5:2479–2497.

Shao, Z., and J. Yang. 1995. Progress in high resolution atomic force microscopy in biology. *Q. Rev. Biophys.* 28:195–251.

Singer, S. J., and G. L. Nicolson. 1972. The fluid mosaic model of the structure of cell membranes. *Science.* 175:720–731.

Sirota, E. B., G. S. Smith, C. R. Safinya, R. J. Plano, and N. A. Clark. 1988. X-ray scattering studies of aligned, stacked surfactant membranes. *Science.* 242:1406–1409.

Soethout, L. L., H. Vankempen, B. J. Nelissen, J. W. Gerritsen, and P. P. M. C. Groenevald. 1988. STM measurements on graphite using correlation averaging of the data. *J. Microsc.* 152:251–258.

Soler, J. M., A. M. Baro, N. Garcia, and H. Rohrer. 1986. Interatomic forces in STM: giant corrugations of graphite. *Phys. Rev. Lett.* 57: 444–447.

Sonnenfeld, R., and P. K. Hansma. 1987. Atomic resolution microscopy in water. *Science.* 232:211–213.

Spong, J. K., H. A. Mizes, L. J. LaComb, Jr., M. M. Dovek, J. E. Frommer, and E. Meyer. 1989. Contrast mechanism for resolving organic molecules with tunnelling microscopy. *Nature.* 338:137–139.

Steere, R. L. 1957. Electron microscopy of structural detail in frozen biological specimens. *J. Biophys. Biochem. Cytol.* 3:45–59.

Stemmer, A., A. Engel, U. Aebi, and A. Hefti. 1989. Scanning tunneling and transmission electron microscopy on identical areas of biological specimens. *Ultramicroscopy.* 30:263–280.

Sun, W. J., S. Tristam-Nagle, R. M. Suter, and J. F. Nagle. 1996. Structure of the ripple phase in lecithin bilayers. *Proc. Natl. Acad. Sci. USA.* 93:7008–7012.

Tardieu, A., V. Luzzati, and F. C. Reman. 1972. Structure and polymorphism of the hydrocarbon chains of lipids: a study of lecithin-water phases. *J. Mol. Biol.* 75:711–733.

Tersoff, J., and N. D. Lang. 1990. Tip dependent corrugation of graphite in scanning tunneling microscopy. *Phys. Rev. Lett.* 65:1132–1135.

Tippmann-Krayer, P., R. M. Kenn, and H. Mohwald. 1992. Thickness and temperature dependent structure of Cd-arachidate Langmuir-Blodgett films. *Thin Solid Films.* 210:577–582.

Travaglini, G., H. Rohrer, M. Amrein, and H. Gross. 1987. Scanning tunneling microscopy on biological matter. *Surfactant Sci.* 181: 380–390.

Wack, D. C., and W. W. Webb. 1989. Synchotron x-ray study of the modulated lamellar phase in the lecithin water system. *Phys. Rev. A.* 40:2712–2730.

Wang, Z. H., T. Hartmann, W. Baumeister, and R. Guckenberger. 1990. Thickness determination of biological samples with a z-calibrated scanning tunneling microscope. *Proc. Natl. Acad. Sci. USA.* 87:9343–9347.

Weigrabe, W., M. Nonnenmacher, R. Guckenberger, and O. Wolter. 1991. Atomic force microscopy of a hydrated bacterial surface protein. *J. Microsc.* 163:79–84.

Weisenhorn, A. L., P. Maivald, H.-J. Butt, and P. K. Hansma. 1992. Measuring adhesion, attraction and repulsion between surfaces in liquids with an atomic-force microscope. *Phys. Rev. B.* 45:11226–11232.

Wepf, R., M. Amrien, U. Burkli, and H. Gross. 1991. Platinum/iridium/carbon: a high-resolution shadowing material for TEM, STM and SEM of biological macromolecular structures. *J. Microsc.* 163:51–64.

Woodward, J. T. 1994. Scanning tunneling microscopy on freeze-fracture replicas of ripple phase of dimyristoylphosphatidylcholine. Ph.D. thesis. University of California, Santa Barbara, CA.

Woodward, J. T., C. Kono, L. L. Madsen, and J. A. Zasadzinski. 1995. Inherent bias in correlation averaged images. *J. Microsc.* 178:86–92.

Woodward, J. T., and J. A. Zasadzinski. 1994. Height amplifications of scanning tunneling microscopy images in air. *Langmuir.* 10:1340–1344.

Woodward, J. T., and J. A. Zasadzinski. 1996a. Amplitude, wave form, and temperature dependence of bilayer ripples in the $P_{\beta'}$ phase. *Phys. Rev. E Rapid Comm.* 53:R3044–R3047.

Woodward, J. T., and J. A. Zasadzinski. 1996b. Thermodynamic limitations on the resolution of metal replicas. *J. Microsc.* (in press).

Woodward, J. T., J. A. Zasadzinski, and P. K. Hansma. 1991. Precision height measurements of freeze-fracture replicas using the scanning tunneling microscope. *J. Vac. Sci. Technol. B.* 9:1231–1235.

Yuan, J.-Y., and Z. Shao. 1990. Simple model of image-formation by scanning tunneling microscopy of nonconducting materials. *Ultramicroscopy.* 34:223–236.

Yuan, J.-Y., Z. Shao, and C. Gao. 1991. Alternative method of imaging surface topologies of nonconducting bulk specimens by scanning tunneling microscopy. *Phys. Rev. Lett.* 67:863–866.

Zasadzinski, J. A. 1988. Effect of stereoconfiguration on ripple phases of dipalmitoylphosphatidylcholine. *Biochim. Biophys. Acta.* 946:235–243.

Zasadzinski, J. A. N., and S. Bailey. 1989. Applications of freeze-fracture replication to problems in materials and colloid science. *J. Electron Microsc. Tech.* 13:309–334.

Zasadzinski, J. A., S. Meiboom, M. J. Sammon, and D. W. Berreman. 1986. Freeze-fracture electron microscope observations of the blue phase III. *Phys. Rev. Lett.* 57:364–367.

Zasadzinski, J. A., and R. B. Meyer. 1986. Molecular imaging of tobacco mosaic virus lyotropic nematic phases. *Phys. Rev. Lett.* 56:636–639.

Zasadzinski, J. A., and M. B. Schneider. 1987. Ripple wavelength, amplitude, and configuration in lyotropic liquid crystals as a function of effective head group size. *J. Phys. (France).* 48:2001–2011.

Zasadzinski, J. A., J. Schneir, J. Gurley, V. Elings, and P. K. Hansma. 1988. Scanning tunneling microscopy of replicas of biomembranes. *Science.* 239:1014–1016.

Zasadzinski, J. A., J. B. Sweeney, H. T. Davis, and L. E. Scriven. 1987. Finite element calculations of fluid menisci and thin films in porous media. *J. Colloid Interface Sci.* 119:108–116.

Zasadzinski, J. A., R. Viswanathan, L. L. Madsen, and D. K. Schwartz. 1994a. Langmuir-Blodgett Films. *Science.* 263:1726–1733.

Zasadzinski, J. A., R. Viswanathan, D. K. Schwartz, J. Garnaes, L. L. Madsen, S. Chiruvolu, J. T. Woodward, and M. L. Longo. 1994b. Applications of AFM to structural characterization of organic thin films. *Colloids Surfaces A.* 93:305–333.